

# Compressive Light Field Imaging

Amit Ashok<sup>a</sup> and Mark A. Neifeld<sup>a,b</sup>

<sup>a</sup>Department of Electrical and Computer Engineering, 1230 E. Speedway Blvd.,  
University of Arizona, Tucson, AZ 85721 USA;

<sup>b</sup> College of Optical Sciences, 1630 E. University Blvd.,  
University of Arizona, Tucson, AZ 85721, USA

## ABSTRACT

Light field imagers such as the plenoptic and the integral imagers inherently measure projections of the four dimensional (4D) light field scalar function onto a two dimensional sensor and therefore, suffer from a spatial vs. angular resolution trade-off. Programmable light field imagers, proposed recently, overcome this spatio-angular resolution trade-off and allow high-resolution capture of the (4D) light field function with multiple measurements at the cost of a longer exposure time. However, these light field imagers do not exploit the spatio-angular correlations inherent in the light fields of natural scenes and thus result in photon-inefficient measurements. Here, we describe two architectures for *compressive* light field imaging that require relatively few photon-efficient measurements to obtain a high-resolution estimate of the light field while reducing the overall exposure time. Our simulation study shows that, compressive light field imagers using the principal component (PC) measurement basis require four times *fewer* measurements and three times *shorter* exposure time compared to a conventional light field imager in order to achieve an equivalent light field reconstruction quality.

**Keywords:** Compressive imaging, Light Field, Principal Component, Hadamard.

## 1. INTRODUCTION

In the computer graphics community the term *light field* refers to the spatio-angular distribution of light rays in free-space emanating from a three-dimensional object volume.<sup>1,2</sup> The light field denoted by  $\ell(x, y, u, v)$  and parametrized by the spatial location  $(x, y)$  and angle/slope  $(u, v)$  of each ray is therefore, a four dimensional scalar quantity. Various optical architectures have been proposed by researchers to measure the 4D light field of a scene, including the well-known plenoptic camera in the computer-graphics community<sup>3-5</sup> and the integral imager in the optics community.<sup>6-8</sup> Both types of imager typically acquire a sampled version of the light field in one snapshot using a two-dimensional detector array such as a CCD or a CMOS image sensor. However, as a light field is a four dimensional function the resulting two-dimensional measurement is typically a “low-resolution” representation with the associated spatial vs. angular resolution trade-off.<sup>9</sup> Some recent studies have reported success in overcoming this spatio-angular resolution trade-off by making a series of two-dimensional measurements, scanning in either angular or spatial dimension of a light field, and synthesizing a higher-resolution light field in post-processing.<sup>10</sup> Note that such a scanning/sampling approach usually requires a large number of measurements and results in long acquisition/exposure times, which can be undesirable in many applications. Perhaps more importantly, such traditional sampling approaches do not exploit the inherent spatio-angular redundancies present in the light field of a natural scene and result in rather photon-inefficient measurements.

In this work, we describe two separate architectures for compressive light field imaging which utilize: 1) the correlation along the angular dimensions of a light field and 2) the correlation along the spatial dimensions of a light field, to make *compressive* measurements towards the goal of synthesizing a high-resolution light field estimate in post-processing. We expect that these angular/spatial correlations will enable light field imaging utilizing fewer photon-efficient compressive measurements and shorter acquisition/exposure time relative to a conventional light field imager employing non-compressive measurements. A simulation study is carried out to

---

Further author information: (Send correspondence to Amit Ashok.)

Amit Ashok: E-mail: ashoka@ece.arizona.edu, Telephone: 1 520 626 4328

Mark A. Neifeld : E-mail: neifeld@ece.arizona.edu, Telephone: 1 520 621 6102

judge the efficacy of the proposed compressive imagers for two choices of compressive measurement bases: a) principal component (PC) and b) Hadamard. The reconstruction performance of the compressive imagers is analyzed along various system parameters, such as number of measurements and length of exposure time, and compared with that obtained from a conventional light field imager.

## 2. ARCHITECTURES FOR COMPRESSIVE LIGHT FIELD IMAGING

We begin by defining a two-plane parametrization of the light field  $\ell(s, t, u, v)$  of a three dimensional object.<sup>11</sup> As shown in Fig. 1, consider  $z = 0$  as the reference  $(s, t)$  plane, an observation plane  $(x, y)$  located at  $z = \Delta z$ , and the  $(u, v)$  plane at  $z = \infty$ . Thus the  $(u, v)$  coordinates represent angles or slopes. A ray emanating from  $(s, t)$  coordinate in the reference plane at slope  $(u, v)$  intersects the observation plane at coordinate  $(x, y)$  where  $x = u\Delta z$  and  $y = v\Delta z$ . Thus each ray can be completely specified by the  $(s, t)$  and  $(u, v)$  coordinates. The light field  $\ell(s, t, u, v)$  is a scalar quantity representing the radiance carried by ray with  $(s, t, u, v)$  coordinates. A careful analysis of the measurable light field shows that it equivalent to the radiance function of a scalar field in a wave-theory interpretation.<sup>11-13</sup> Ref. [11] provides an excellent review of light fields from the wave-theory perspective.

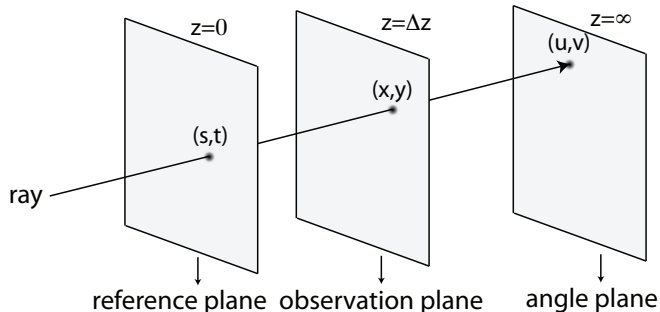


Figure 1. Two-plane ray parametrization.

The two traditional optical architectures for measuring the light field of an object are shown in Fig. 2. Note that in the case of the plenoptic camera the size of each lenslet together with the number of detector elements in the image sensor determines the angular and spatial resolution of the light field measurement. Suppose the image sensor has  $N \times N$  detector elements and the size of each lenslet is equivalent to  $K$  detector elements, then the resulting light field measurement will have  $\lfloor N/K \rfloor \times \lfloor N/K \rfloor$  resolution elements in the spatial dimension and  $K \times K$  resolution elements in the angular dimension. Therefore, increasing the lenslet size decreases the spatial resolution while improving the angular resolution of the light field and vice versa. Note that the total number of resolution elements in the measured light field remains fixed at  $N \times N$ . In the case of an integral imager a complimentary trade-off is found in which increasing the lenslet size increases the spatial resolution at the cost of decreasing the angular resolution.

It may argued that one can increase the light field resolution along both angular and spatial dimensions by simply using smaller lenslets and smaller detector elements. However, such an approach would quickly reduce the measurement signal to noise ratio (SNR), for a fixed exposure time, thereby degrading the light field fidelity. An implementation of a similar approach using multiple data acquisitions employing an extended total exposure time has been recently reported in Ref.[10]. In this particular measurement scheme, shown in Fig. 3, the spatial component  $\ell(s, t, u_i, v_i)$  of the light field is estimated at full sensor resolution  $N \times N$  for each angular coordinate  $(u_i, v_i)$  with a conventional imager employing an amplitude-mask in its lens aperture. This amplitude-mask may be implemented via a programmable spatial light modulation (SLM) such as a liquid crystal SLM (LC-SLM). By scanning through various configurations of the amplitude-mask, defined on a  $K \times K$  grid, a high-resolution light field with dimensions  $(N \times N, K \times K)$  is synthesized using  $K^2$  measurements. This requires a total exposure time that is  $K^2$  times the exposure time of a single-shot low-resolution measurement obtained with either a plenoptic or an integral imager. Our first compressive light field imager utilizes this architecture and is described in following sub-section.

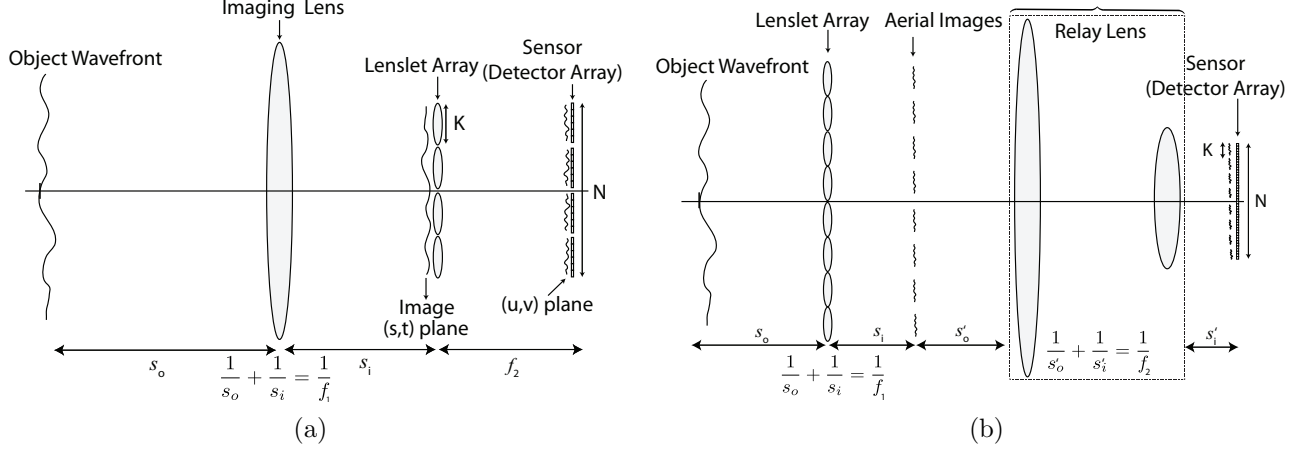


Figure 2. Architecture of traditional light field imager: (a) Plenoptic camera and (b) Integral imager.

## 2.1 Angular Compressive Light Field (ACLF) Imager

The  $k^{th}$  image measurement  $\mathbf{g}_k^{ang}$  ( $N \times N$  matrix) corresponding to the  $k^{th}$  amplitude-mask configuration, denoted by  $\mathbf{P}_k^{ang}$  ( $K \times K$  matrix), can be expressed as

$$\mathbf{g}_k^{ang} = [P_k^{ang}(1,1)\mathbf{I}_{N \times N} \dots P_k^{ang}(i,j)\mathbf{I}_{N \times N} \dots P_k^{ang}(K,K)\mathbf{I}_{N \times N}] \cdot [\ell(:, :, 1, 1) \dots \ell(:, :, i, j) \dots \ell(:, :, K, K)]^T + \mathbf{n}_k, \quad (1)$$

where  $P_k^{ang}(i,j)$  is the  $(i,j)$  element of the  $\mathbf{P}_k^{ang}$  matrix,  $\mathbf{I}_{N \times N}$  is a  $N \times N$  identity matrix,  $\ell(:, :, i, j)$  is the spatial image of size  $N \times N$  corresponding to angular coordinate  $(u_i, v_i)$  of the light field and  $\mathbf{n}_k$  represents the measurement noise matrix of size  $N \times N$ . From Eq. (1), we observe that the pixel at location  $(m,n)$  of the image measurement  $\mathbf{g}_k^{ang}$  can be expressed compactly as

$$g_k^{ang}(m, n) = \mathbf{P}_k^{ang} \cdot \ell^{ang}(m, n) + n_k(m, n), \quad (2)$$

where  $\ell^{ang}(m, n) = \ell(m, n, :, :)$  is the angular sub-component of size  $(K \times K)$  corresponding to spatial coordinate  $(s_m, t_n)$  of the light field and  $n_k(m, n)$  is the measurement noise at pixel location  $(m, n)$  in the  $k^{th}$  image measurement. Observe the pixel at location  $(m,n)$  of the  $k^{th}$  image measurement  $g_k^{ang}(m, n)$ , is a projection of the angular sub-component of the light field  $\ell^{ang}(m, n)$  onto the  $k^{th}$  amplitude-mask projection matrix  $\mathbf{P}_k^{ang}$ . Arranging, the first  $M$  image measurement pixels at location  $(m, n)$  into a vector  $\vec{g}^{ang}(m, n)$  of length  $M$  we get

$$\vec{g}^{ang}(m, n) = \mathbf{P}^{ang} \cdot \vec{\ell}^{ang}(m, n) + \vec{n}(m, n), \quad (3)$$

where  $\mathbf{P}^{ang}$  is a  $M \times K^2$  projection matrix whose  $k^{th}$  row vector is obtained by lexicographically arranging the  $k^{th}$  amplitude-mask  $\mathbf{P}_k^{ang}$ . The light field vector  $\vec{\ell}^{ang}(m, n)$  of length  $K^2$  is obtained by lexicographically arranging the angular sub-component  $\ell^{ang}(m, n)$  and noise vector  $\vec{n}(m, n)$  of length  $M$  consists of measurement noise at pixel location  $(m, n)$  in the  $M$  image measurements.

The light field measurement scheme reported in Ref. [10], makes  $M = K^2$  measurements using two different measurement bases: 1) identity basis (i.e.  $\mathbf{P}^{ang} = \mathbf{I}_{K^2 \times K^2}$ ) and 2) a SNR optimized basis. Here we consider a *compressive* measurement scheme where the number of measurements  $M$  is *less* than the light field angular dimensionality  $K^2$ . Note that this measurement scheme is only compressive in the angular dimension of the light field and does not exploit any spatial correlation or sparsity information for compressive measurements. In the next sub-section we describe a compressive Plenoptic light field imager which makes compressive measurements along the spatial dimension of a light field.

## 2.2 Spatial Compressive Light Field (SCLF) Imager

As discussed earlier, the spatial resolution of a light field is limited by the lenslet size/pitch in the Plenoptic camera, shown in Fig. 2 (a). To understand this more clearly, let us consider the sensor measurement behind

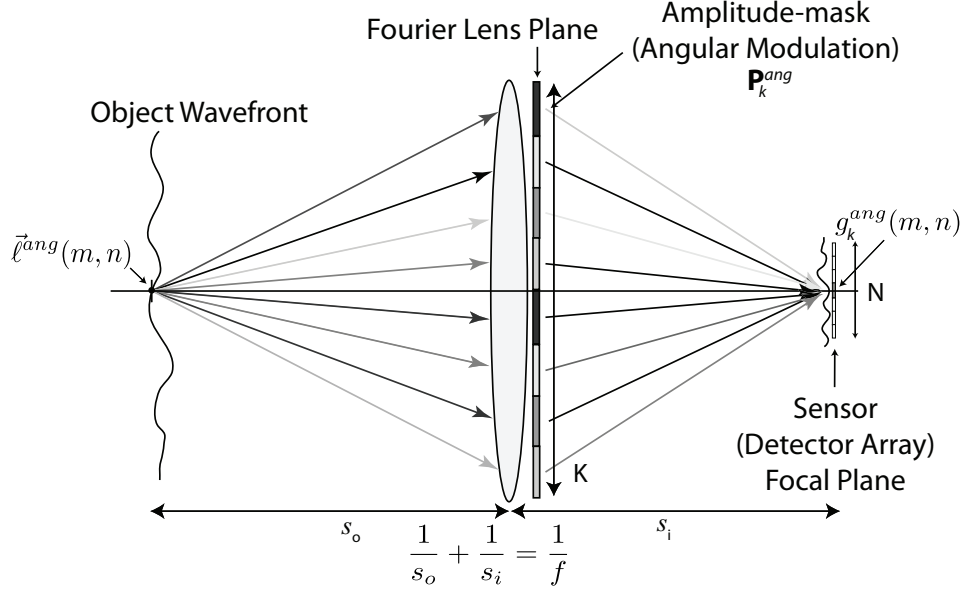


Figure 3. Angular compressive light field imager architecture.

one lenslet at location  $(i, j)$ . Mathematically, the  $K \times K$  sensor measurement, denoted by vector  $\vec{g}^{spt}(i, j)$  (lexicographically ordered), is given by

$$\vec{g}^{spt(i,j)} = \mathbf{1}_{K^2} \cdot \left[ \vec{\ell}^{spt(i,j)}(1,1)^T \vec{\ell}^{spt(i,j)}(1,2)^T \dots \vec{\ell}^{spt(i,j)}(m,n)^T \dots \vec{\ell}^{spt(i,j)}(K,K)^T \right] + \vec{n}^{(i,j)}, \quad (4)$$

where the square lenslet spans  $K$  detectors in each direction,  $\mathbf{1}_{K^2}$  is an all one row vector of length  $K^2$ ,  $\vec{\ell}^{spt(i,j)}(m, n) = [\ell(i-K/2, j-K/2, m, n) \ell(i-K/2+1, j-K/2, m, n) \dots \ell(i, j, m, n) \dots \ell(i+K/2-1, j+K/2-1, m, n)]$  and  $\vec{n}^{(i,j)}$  is the measurement noise vector of length  $K^2$ . Thus, from Eq. (4) we infer that the sensor behind each lenslet measures the angular sub-component of the light field that has been spatially integrated over the full extent of that lenslet.

Now let us consider a case where we place an amplitude-mask over a lenslet (defined over a  $K \times K$  grid) as shown in Fig. 4. This amplitude-mask may be implemented via a programmable LC-SLM or a digital mirror array device (DMD). The resulting sensor measurement  $\vec{g}_k^{spt(i,j)}$  corresponding to the  $k^{th}$  configuration of the amplitude-mask, defined by a  $K \times K$  matrix  $\mathbf{P}_k^{spt}$ , can be expressed as

$$\vec{g}_k^{spt(i,j)} = \vec{P}_k^{spt} \left[ \vec{\ell}^{spt(i,j)}(1,1)^T \quad \vec{\ell}^{spt(i,j)}(1,2)^T \quad \dots \quad \vec{\ell}^{spt(i,j)}(m,n)^T \quad \dots \quad \vec{\ell}^{spt(i,j)}(K,K)^T \right] + \vec{n}_k^{(i,j)}, \quad (5)$$

where the row vector  $\vec{P}_k^{spt}$  of length  $K^2$  is obtained by lexicographically arranging matrix  $\mathbf{P}_k^{spt}$ . Examining the pixel at location  $(m, n)$  in the sensor measurement, we can express it as

$$g_k^{spt(i,j)}(m, n) = \vec{P}_k^{spt} \cdot \vec{\ell}^{spt(i,j)}(m, n)^T + n_k^{(i,j)}(m, n). \quad (6)$$

Scanning the amplitude-mask through  $M$  distinct configurations yields a measurement vector  $\vec{g}^{spt(i,j)}(m, n)$  of length  $M$  defined as

$$\vec{g}^{spt(i,j)}(m, n) = \mathbf{P}^{spt} \cdot \vec{\ell}^{spt(i,j)}(m, n)^T + \vec{n}^{(i,j)}(m, n), \quad (7)$$

where  $\mathbf{P}^{spt}$  is the  $M \times K^2$  projection matrix whose  $k^{th}$  row vector is  $\vec{P}_k^{spt}$  and  $\vec{n}^{(i,j)}(m, n)$  is the corresponding measurement noise vector of length  $M$ . Note that this measurement vector  $\vec{g}^{spt(i,j)}(m, n)$  at pixel location  $(m, n)$  is a projection of the local (at location  $(i, j)$ ) spatial sub-component of the light field  $\vec{\ell}^{spt(i,j)}(m, n)$  onto the measurement basis defined by projection matrix  $\mathbf{P}^{spt}$ . Here we consider a *compressive* measurement scheme where the number of measurements  $M$  is *less* than the dimensionality ( $K^2$ ) of the local light field  $\vec{\ell}^{spt(i,j)}(m, n)$ .

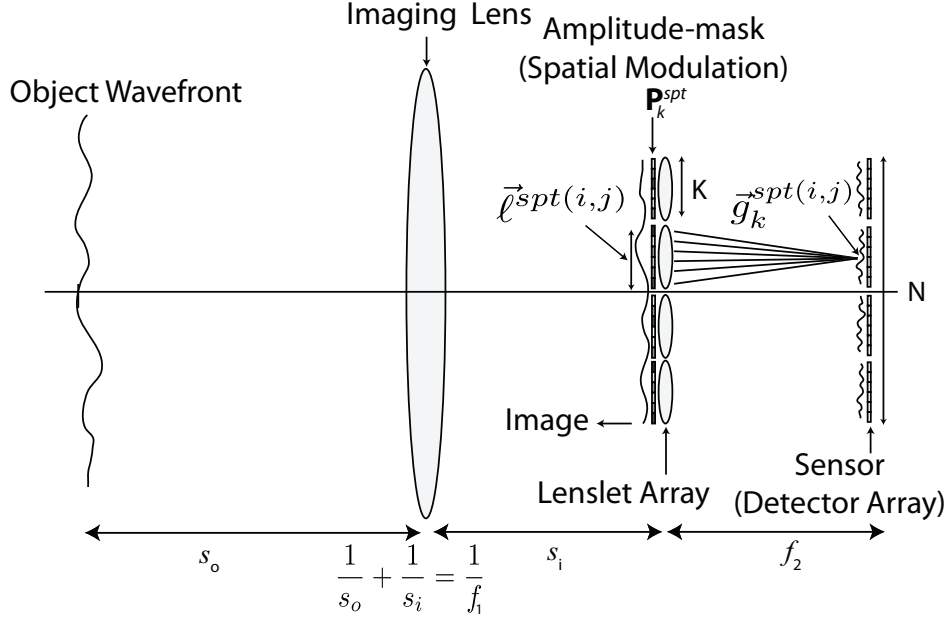


Figure 4. Spatial compressive light field imager architecture.

Examining, Eq. (7) closely reveals that this measurement scheme is only compressive along the local spatial-dimension of the light field and therefore, does not exploit any angular correlation or sparsity information for compressive measurements. Here we use the same amplitude-mask for each lenslet. This implies that each pixel within the sensor measurement employs the same measurement basis  $\mathbf{P}^{spt}$ .

Both the compressive light field imaging architectures described here employ  $M$  compressive light field measurements within a total exposure time of  $T^{exp} = L \times T_0^{exp}$ . Here  $T_0^{exp}$  corresponds to the exposure time associated with a single traditional measurement without an amplitude-mask, thus  $L$  indicates the number of such  $T_0^{exp}$  exposure times that comprise the total exposure time  $T^{exp}$ . For any  $L > 1$  this means that the total exposure time required by the compressive light field imager is  $L$  times longer than the traditional single-shot light field imager. It is also important to note that  $T^{exp}$  remains constant as  $M$  changes which has important measurement  $SNR$  implications.

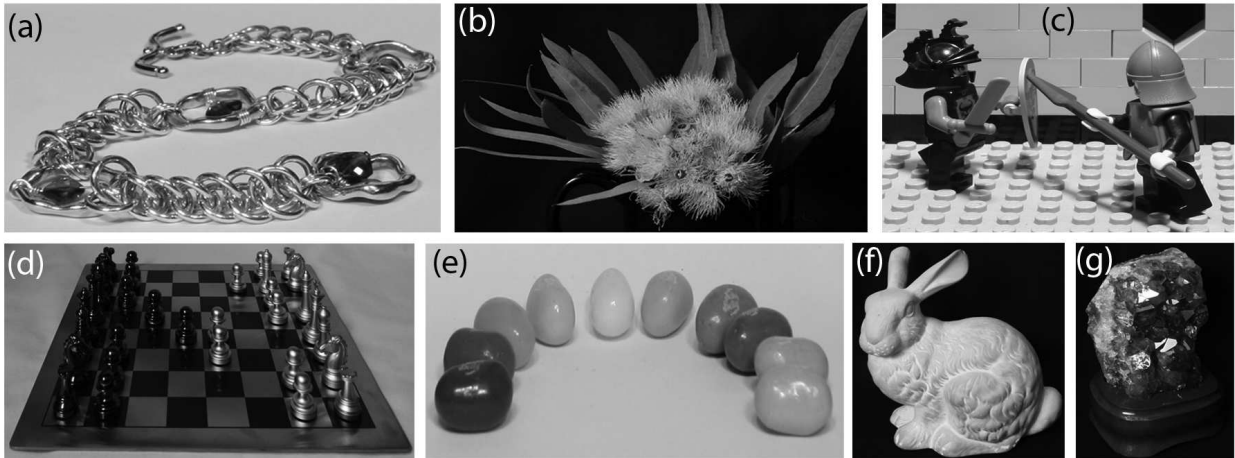


Figure 5. Light field dataset used in the simulation study: (a), (b), (c), (f), (g) comprise the *training* dataset and (d), (e) comprise the *testing* dataset.

### 3. RESULTS AND DISCUSSION

The choice of the measurement basis is a key factor in determining the performance of a compressive imager. Here we quantify the reconstruction performance of the compressive light field imagers for two choices of measurement basis: 1) principal component (PC) or Karhunen-Loève basis and 2) binary Hadamard basis. The motivation behind using the PC basis is that it provides information-optimal compression for Gaussian sources. We expect that this choice of basis will exploit the inherent spatial/angular correlations (up to the second order) in the light field to yield a sparse representation. On the other hand the Hadamard basis, though not as efficient as the PC basis for compressing data, is chosen primarily for its photon-throughput efficiency (i.e. ratio of incident irradiance transmitted through amplitude-mask). In this work, we use a training dataset composed of five high-resolution light fields shown in Fig. 5, chosen from the Stanford’s light field archive<sup>14</sup>, to compute the projection matrix that defines the PC basis. Note that the angular size of the light fields used in this study is  $8 \times 8$  ( $K = 8$ ).

For the ACLF imager, eigenvectors of the autocorrelation matrix of the angular component of the light field comprise the PC projection matrix of size  $64 \times 64$ . The row vectors of the PC projection matrix are arranged according to decreasing eigenvalues, thus the first row vector corresponds to the highest eigenvalue. Fig. 6(a) shows the first 16 PC projection vectors arranged in decreasing order from left to right and from top to bottom. Similarly, Fig. 6(b) shows the first 16 Hadamard projection vectors arranged in the same manner. In case of the Hadamard projection matrix, the row vectors are sorted in order of decreasing inner product between a row vector and a light field sample, averaged over the training dataset ensemble.

Note that because the PC and Hadamard projection matrices contain negative elements that cannot be physically implemented using an amplitude-only mask, we use the dual-rail measurement scheme described in Ref. [15]. To ensure that the total number of photons remains fixed for each imager and for all choices of  $M$ , we scale the positive and negative components of the  $k^{th}$  row vector of a PC/Hadamard projection matrix  $\mathbf{P}^{ang}$  as follows

$$\vec{P}_+^{ang}(k) = \alpha_{split} \frac{L}{K^2} (\vec{P}_+^{ang}(k)/C_k^+) \quad (8)$$

$$\vec{P}_-^{ang}(k) = (1 - \alpha_{split}) \frac{L}{K^2} (\vec{P}_-^{ang}(k)/C_k^-) \quad (9)$$

where  $\alpha_{split}$  is the power-splitting ratio associated with the dual-rail implementation,  $L$  is the multiplicative factor in the total exposure time  $T^{exp}$ ,  $C^+(k)/C^-(k)$  is the absolute maximum value of the  $\vec{P}_+^{ang}(k)/\vec{P}_-^{ang}(k)$  positive/negative  $k^{th}$  row vector. Here we set  $\alpha_{split} = 0.5$  so that the positive/negative measurement use equal

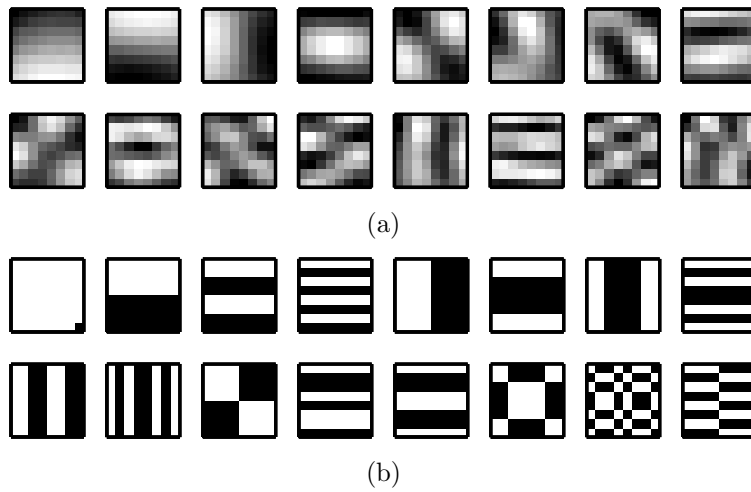


Figure 6. First 16 projection vectors from (a) PC measurement basis and (b) Hadamard measurement basis, shown here as  $8 \times 8$  images.

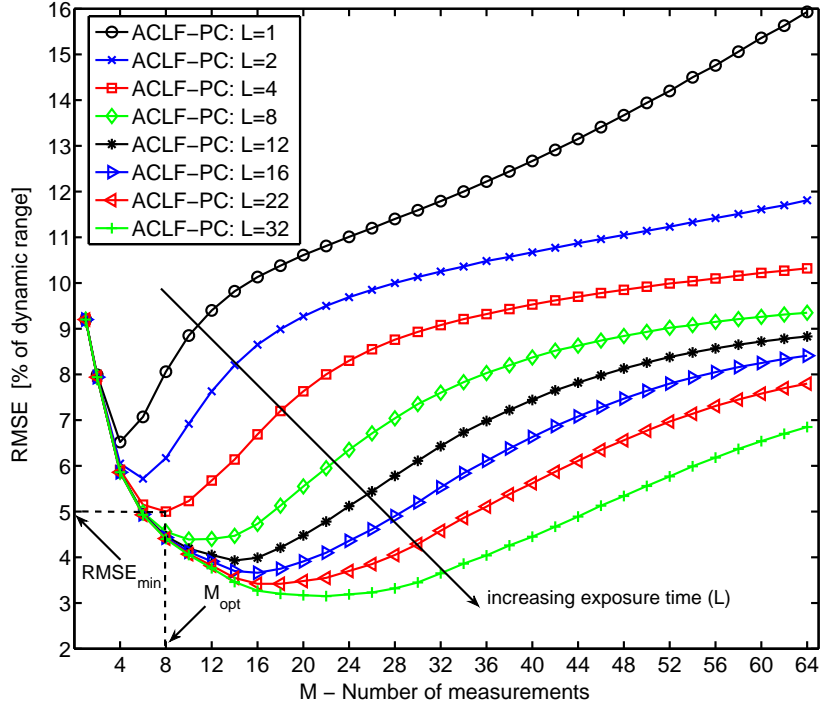


Figure 7. RMSE performance of ACLF-PC imager as function of  $M$  for various exposure times specified by  $L$ .

exposure time. Also note that the scaling specified in Eqs. (8) and (9) implies that each compressive measurement uses an equal exposure time. To reconstruct the light field data from the  $M$  compressive measurements we use the the linear minimum mean square error (LMMSE) operator  $\mathbf{W}^{ang}$  that is defined as

$$\mathbf{W}^{ang} = \mathbf{R}_{\ell\ell}^{ang} \mathbf{P}^{ang T} (\mathbf{P}^{ang} \mathbf{R}_{\ell\ell}^{ang} \mathbf{P}^{ang T} + \mathbf{R}_{nn})^{-1}, \quad (10)$$

where  $\mathbf{R}_{\ell\ell}^{ang}$  is the autocorrelation matrix of the angular component of the light field data and  $\mathbf{R}_{nn}$  is the autocorrelation matrix of the detector noise vector. To quantify the performance of the ACLF imagers we use two light field samples from the testing dataset, shown in Fig. 5, that are distinct from the training dataset. The normalized root mean square error (RMSE) metric (expressed as a percentage of the dynamic range) is used to quantify the quality of the light field estimates. Here we use an additive white Gaussian noise (AWGN) model to represent the detector noise in the measurement process. The noise standard deviation is set to  $\sigma_n = 1$  where the dynamic range (DR) of the sensor is  $[0 - 1023]$  (10-bit quantization).

Figure 7 shows a plot of the reconstruction RMSE as a function of number of measurements  $M$  for the ACLF-PC imager (PC basis). Note that the RMSE decreases initially with increasing  $M$  reaching a minima and then starts to increase. There are two underlying mechanisms that determine this behavior of RMSE with  $M$ : 1) truncation error 2) measurement SNR. The truncation error reduces with increasing  $M$  as more coefficients are used to represent the light field. However, given the fixed exposure time, the signal energy in each measurement decreases with increasing  $M$  and together with fixed detector noise this has the implication of reduced measurement SNR. Thus the minimum RMSE is achieved when these two competing mechanisms balance each other at  $M_{opt}$  number of measurements. Observe that as  $L$  increases (i.e. exposure time increases) a lower minimum RMSE is achieved at larger values of  $M_{opt}$  as a result of increased signal energy and reduced truncation error. Comparing the ACLF-PC imager performance with that of a conventional light field (CONV) imager (where  $\mathbf{P}^{ang} = \mathbf{I}$  and  $M = K^2 = 64$ ) at various exposure times shows nearly one to two orders of magnitude improvement for small values of  $L$ . This is evident from the RMSE performance of the ACLF and CONV imagers summarized in Table 1. For instance at  $L = 1$ , the ACLF-PC imager yields a RMSE= 6.5% with

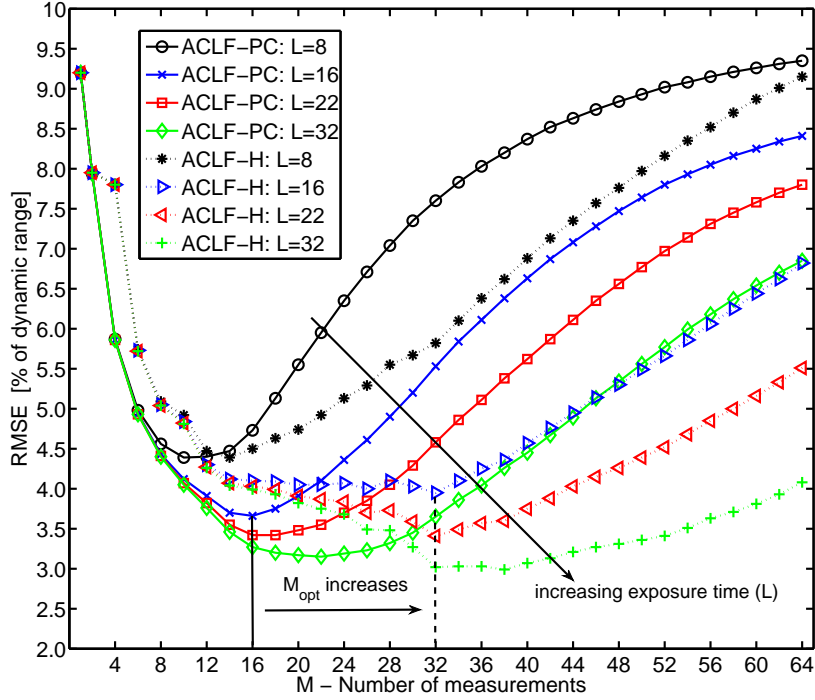


Figure 8. RMSE performance of ACLF-PC and ACLF-H imagers as function of  $M$  for four exposure times specified by  $L$ .

$M_{opt} = 3$  as compared to  $\text{RMSE}=400\%$  for the CONV imager. Increasing the total exposure time by a factor of  $L = 16$  results in a lower  $\text{RMSE}=3.7\%$  for ACLF-PC imager obtained with  $M_{opt} = 16$  measurements which is still nearly an order of magnitude less than  $\text{RMSE}=25\%$  of the CONV imager.

Figure 8 shows a plot of the reconstruction RMSE vs.  $M$ , comparing the relative performance of the ACLF-PC and ACLF-H imagers using the PC and the Hadamard basis respectively. Here we observe that for nearly all values of  $L$  the ACLF-PC imager outperforms the ACLF-H imager in terms of the number of measurements  $M_{opt}$  required to reach the minimum RMSE (refer to data in Table 1). This is due to the superior compressibility of the PC basis despite its slightly inferior photon-throughput efficiency. For example, at  $L = 16$  the ACLF-PC imager achieves the minimum RMSE at  $M_{opt} = 16$  as opposed to  $M_{opt} = 26$  for the ACLF-H imager. However, as the total exposure time increases with  $L$  and the measurement SNR improves leading to higher  $M_{opt}$  (i.e. lower compression), the performance gap between ACLF-PC and ACLF-H narrows as the photon-throughput advantage of the Hadamard basis becomes more dominant. It is also interesting to compare the relative performance of these two imagers operating in non-compressive mode i.e. where  $M = 64 = K^2$ . The RMSE data in the last three rows of Table 1 shows that the Hadamard basis always achieves the best performance

Table 1. RMSE performance of ACLF imagers, operating in compressive and non-compressive modes, and the CONV imager.

RMSE ↓ / Exposure Time →	L=1	L=8	L=16	L=22	L=32	L=64
Compressive ACLF-PC( $M_{opt}$ )	6.5%(3)	4.35%(13)	3.7%(16)	3.4%(17)	3.15%(22)	2.6%(30)
Compressive ACLF-H( $M_{opt}$ )	6.7%(5)	4.4%(14)	4.0%(26)	3.5%(35)	3.0%(35)	2.1%(60)
Non-Compressive ACLF-PC( $M = 64$ )	15.9%	9.35%	8.4%	7.8%	6.85%	4.6%
Non-Compressive ACLF-H( $M = 64$ )	15.7%	9.15%	6.8%	5.5%	4.1%	2.2%
CONV ( $M = 64$ )	400%	50%	25%	18%	12.5%	6.25%

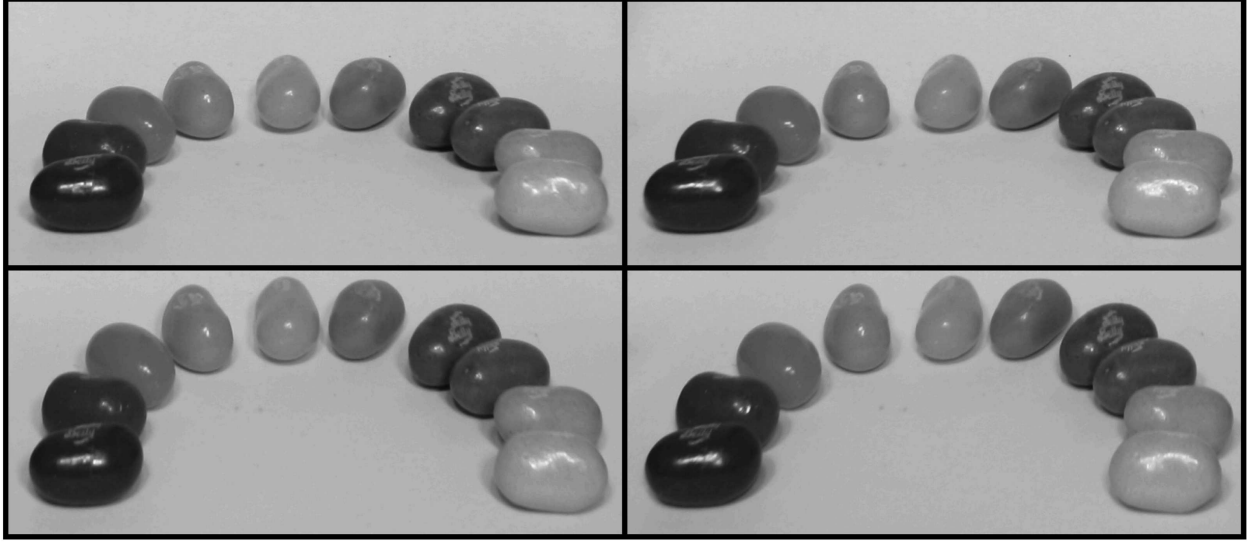
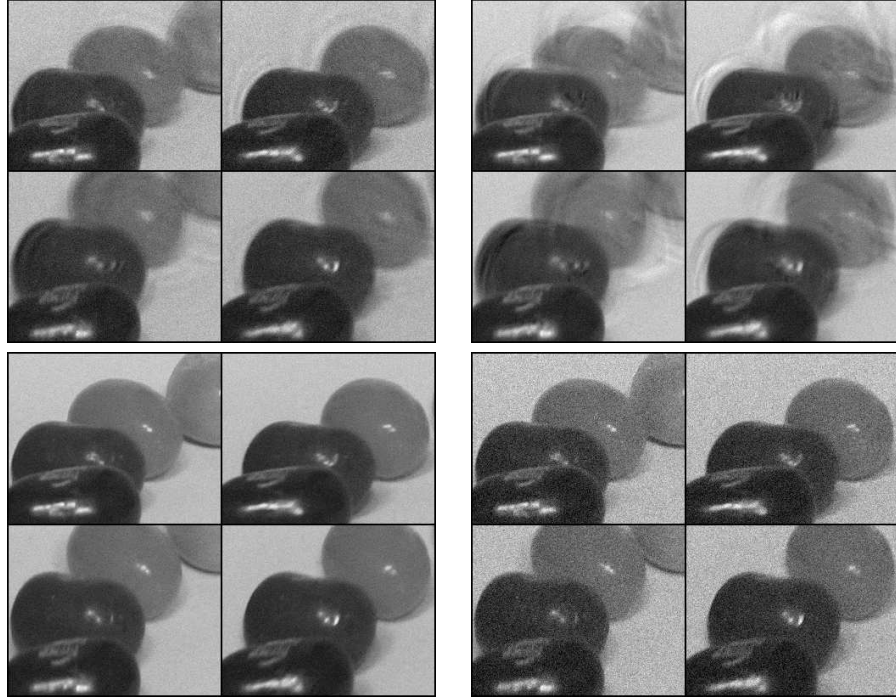


Figure 9. Reference light field images used in simulation at four different angular positions: top left at  $(m = 0, n = 0)$ , top right at  $(m = 0, n = 8)$ , bottom left is at  $(m = 8, n = 0)$  and bottom right is at  $(m = 8, n = 8)$ . Note the horizontal and the vertical parallax in these images.

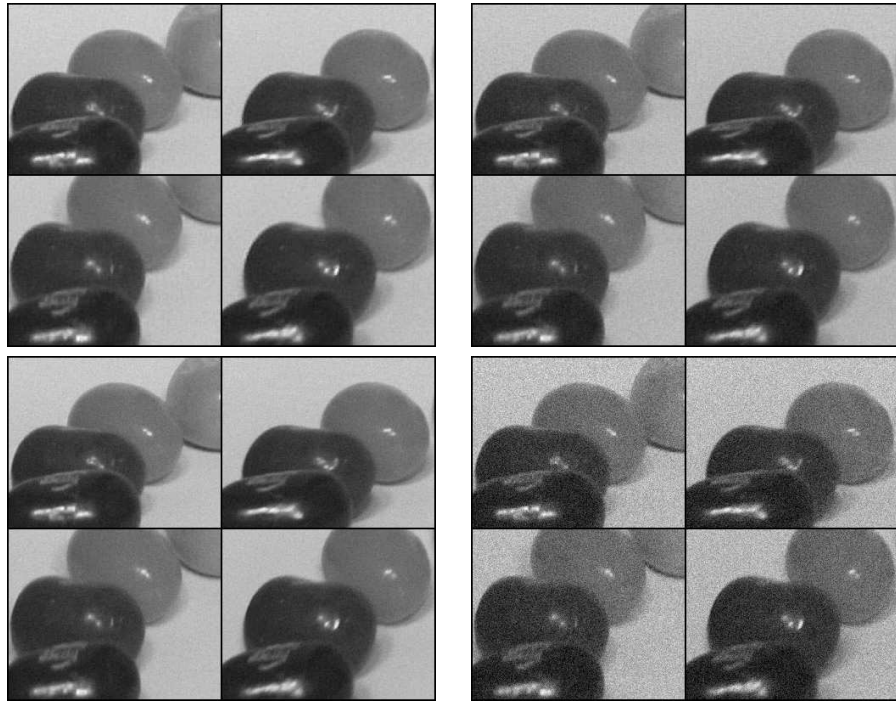
among all three basis (PC, Hadamard, and identity for CONV) due to its superior light throughput efficiency. Therefore, if reduced exposure time is of primary importance in a particular application and the number of measurement is not critical, then ACLF-H imager offers the best performance. The ACLF-H imager at  $L = 16$  achieves nearly the same reconstruction performance as a CONV imager at  $L = 64$ , this represents a four times reduction in the total exposure time.

So far we have presented a quantitative analysis of the ACLF and the CONV imagers. As light fields are often used in visual applications it is also important to provide a visual image-quality based qualitative comparison of the light field reconstructions. Figure 9 shows the reference light field images, representing the object light field, at four different angular locations. Figure 10(a) shows a selected (and magnified) portion of the corresponding reconstructed light field images for the ACLF-PC, ACLF-H and the CONV imagers. Observe that the ACLF-PC imager with  $M = 22$  and  $L = 16$  offers comparable visual image-quality light field images (although some ringing artifacts are visible) as the CONV imager that requires a four times longer exposure time and three times more measurements i.e. ( $M = 64$  and  $L = 64$ ). This highlights the potential for improved performance achievable with the ACLF imagers. Note that the light field images from the ACLF-H imager show significant ringing artifacts indicating relatively poor compressibility on this particular light field using the Hadamard basis.

Next, we consider the spatial compressive light field (SCLF) imager described in sub-section 2.2. Here we use the same training and testing light field datasets from the ACLF study. In case of the SCLF-PC imager, the row vectors of the PC projection matrix correspond to eigenvectors of the autocorrelation matrix estimated using the spatial component of the light fields from the training dataset. The row vectors of the Hadamard projection matrix in the SCLF-H imager are sorted in a manner identical to that described in case of the ACLF-H imager. A plot of the reconstruction RMSE vs.  $M$  for the SCLF-PC and SCLF-H imagers is shown in Fig. 11 for four values of  $L$ . The performance trends, qualitatively similar to those for ACLF imagers, indicate the superior performance of the SCLF-PC imager relative to the SCLF-H imager in terms of the number of measurements  $M_{opt}$  required to achieve the minimum RMSE. For example with  $L = 16$ , the SCLF-PC imager requires  $M_{opt} = 11$  compared to  $M_{opt} = 23$  for the SCLF-H imager to achieve the minimum RMSE. Table 2 summarizes the RMSE performance of the SCLF and CONV imagers. It is interesting to compare the RMSE performance of the ACLF and SCLF imagers for the same measurement basis. We note in the case of the SCLF-PC imager the RMSE performance is better than that of ACLF-PC by nearly a factor of two for small values of  $L$ . For instance with  $L = 16$ , SCLF-PC achieves the minimum RMSE=2.35% at  $M_{opt} = 11$  compared to RMSE=3.7% at  $M_{opt} = 16$  for



(a)



(b)

Figure 10. Light field image reconstructions: (a) ACLF architecture: top row (compressive:  $M \ll 64, L = 16$ ) - left image from ACLF-PC with  $M = 22$ , right image from ACLF-H with  $M = 26$  and bottom row (non-compressive:  $M = 64, L = 64$ ) - left image from ACLF-H and right image from CONV. (b) SCLF architecture: top row (compressive:  $M \ll 64, L = 16$ ) - left image from SCLF-PC with  $M = 11$ , right image from SCLF-H with  $M = 22$  and bottom row (non-compressive:  $M = 64, L = 64$ ) - left image from SCLF-H and right image from CONV.

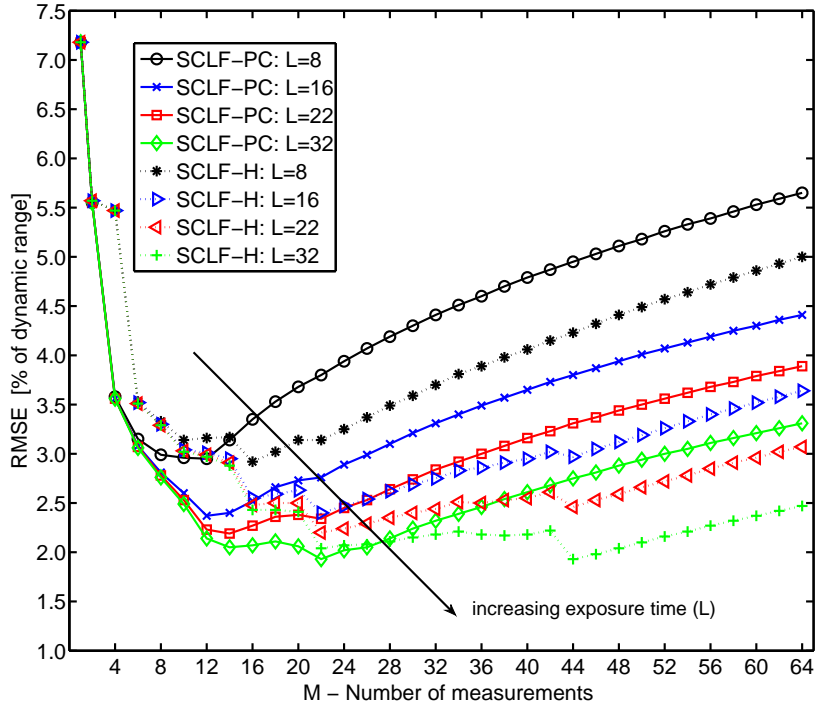


Figure 11. RMSE performance of SCLF-PC and SCLF-H imagers as function of  $M$  for four exposure times specified by  $L$ .

ACLF-PC imager. This suggests superior compressibility in the PC basis for the spatial component compared to the angular component of a light field, at least in the case of the datasets used in this work. A visual inspection of the light field reconstructions, shown in Fig. 10(b), obtained with the SCLF-PC and the SCLF-H imagers confirms this observation. The ringing artifacts visible in the ACLF reconstruction are nearly non-existent in the case of the SCLF reconstruction. Also note that the SCLF imagers require *fewer* compressive measurements to achieve the same RMSE compared to the ACLF imagers.

Table 2. RMSE performance of SCLF imagers, operating in compressive and non-compressive modes, and the CONV imager.

RMSE ↓ / Exposure Time →	L=1	L=8	L=16	L=22	L=32	L=64
Compressive SCLF-PC( $M_{opt}$ )	4.3%(3)	3.0%(8)	2.35%(11)	2.2%(14)	1.9%(22)	1.4%(27)
Compressive SCLF-H( $M_{opt}$ )	4.3%(5)	2.9%(16)	2.4%(23)	2.2%(23)	1.9%(44)	1.2%(44)
Non-Compressive SCLF-PC( $M = 64$ )	14.2%	5.65%	4.4%	3.9%	3.3%	2.3%
Non-Compressive SCLF-H( $M = 64$ )	14.0%	5.0%	3.6%	3.1%	2.5%	1.55%
CONV ( $M = 64$ )	400 %	50%	25%	18%	12.5%	6.25%

#### 4. CONCLUSIONS AND FUTURE WORK

We have described two architectures for compressive light field imaging which exploit the inherent redundancies along the angular and the spatial dimension of a light field. The simulated performance of these compressive imagers confirm the presence of strong angular and spatial correlations in light fields evident from the significant reduction in number of measurements required by these imagers compared to a conventional imager. All the compressive light field imagers presented here (ACLF-PC, ACLF-H, SCLF-PC, SCLF-H) yield one to two orders of magnitude of performance improvements compared to a conventional imager for short exposure times.

Although the performance gap between the compressive imagers and a conventional imager reduces with increasing exposure time, the compressive imagers still maintain a significant performance advantage. At  $L = 32$ , for example the SCLF-PC imager still achieves a significantly lower RMSE=1.9% compared to RMSE=12.5% for the conventional imager. We observed that operating in even a non-compressive mode the ACLF and SCLF imagers offer significant performance improvement and achieve equivalent performance as a conventional imager with an exposure time that is a factor of three to four times smaller. Results from our simulation study have motivated us to implement the compressive imagers described here with goal of experimentally validating the predicted performance improvements. We are currently in the process of implementing a compressive light field imager and plan to report the experimental results in a future communication. Another area that requires further attention is the development of a more accurate model of a compressive imager accounting for the various non-idealities typically associated with a physical implementation, such as non-uniformities in the SLM device (LC-SLM and/or DMD). Note that the class of compressive imagers presented in this work achieves compression in either spatial or angular dimension of a light field. We believe that it is possible to further improve the compressive performance by exploiting the joint spatio-angular correlations present in the light field. Moreover, by employing a hybrid measurement basis described in Ref. [16] we can extend the use of a compressive light field imager over a wider class of natural scenes. This is a direction of research we actively pursuing.

## REFERENCES

1. A. Gershun, "The light field," (translated by P. Moon and G. Timoshenko) *J. Math. and Physics*, 18, pp. 51-151, 1939.
2. M. Levoy and P. Hanrahan, "Light field rendering," in *Proc. ACM SIGGRAPH*, 1996.
3. T. Adelson and J. Wang, "Single Lens Stereo with a Plenoptic Camera," *IEEE Trans. Pattern Analysis and Machine Intelligence*, 14(2), pp. 99-106, 1992.
4. R. Ng, M. Levoy, M. Brédif, G. Duval, M. Horowitz, and P. Hanrahan, "Light field photography with a hand-held plenoptic camera," Technical Report CTSR 2005-02, Stanford University, 2005.
5. M. Levoy, R. Ng, A. Adams, M. Footer, and M. Horowitz, "Light Field Microscopy," *ACM Trans. Graphics*, 25(3), pp. 924 - 934, 2006.
6. G. Lippmann, "La photographie integrale," *C. R. Acad. Sci.* 146, 446-451, 1908.
7. S. Hong, J. Jang, and B. Javidi, "Three-dimensional volumetric object reconstruction using computational integral imaging," *Optics Express*, 12, pp. 483-491, 2004.
8. B. Javidi, I. Moon, and S. Yeom, "Three-dimensional identification of biological microorganism using integral imaging," *Optics Express*, 14, pp. 12096-12108, 2006.
9. T. Georgiev, K. Zheng, B. Curless, D. Salesin, S. Nayar, "Spatio-Angular Resolution Tradeoff in Integral Photography," in *Proceedings of Eurographics Symposium on Rendering*, 2006.
10. C. K. Liang, T. H. Lin, B. Y. Wong, C. Liu, and H. H. Chen, "Programmable aperture photography: multiplexed light field acquisition," *ACM Trans. Graph.*, pp. 1-10, 2008.
11. Z. Zhang and M. Levoy, "Wigner distributions and how they relate to the light field," in *Proceedings of ICCP'09 (IEEE)*, 2009.
12. A. Walther, "Radiometry and coherence," *J. Opt. Soc. Am.*, 58(9), pp. 1256 - 1259, 1968.
13. E. Wolf, "Coherence and radiometry," *J. Opt. Soc. Am.*, 68(1), pp. 6 -17, 1978.
14. The (New) Stanford Light Field Archive, <http://lightfield.stanford.edu/index.html>
15. M. Neifeld and P. Shankar, "Feature specific imaging," *Applied Optics*, 42(17), pp. 3379-3389, 2003.
16. A. Ashok and M. Neifeld, "Compressive Imaging: Hybrid Projection Design," in *Proceedings of Imaging Systems topical meeting, OSA*, 2010.